



HAL
open science

Fatigue properties of as-built and heat-treated Inconel 625 obtained by the hybridization of two laser-powder based additive processes

Noémie Martin, Anis Hor, Etienne Copin, Philippe Lours, Léon Ratsifandrihana

► **To cite this version:**

Noémie Martin, Anis Hor, Etienne Copin, Philippe Lours, Léon Ratsifandrihana. Fatigue properties of as-built and heat-treated Inconel 625 obtained by the hybridization of two laser-powder based additive processes. *International Journal of Fatigue*, 2023, 172, pp.107650. 10.1016/j.ijfatigue.2023.107650 . hal-04051964

HAL Id: hal-04051964

<https://imt-mines-albi.hal.science/hal-04051964>

Submitted on 31 Mar 2023

HAL is a multi-disciplinary open access archive for the deposit and dissemination of scientific research documents, whether they are published or not. The documents may come from teaching and research institutions in France or abroad, or from public or private research centers.

L'archive ouverte pluridisciplinaire **HAL**, est destinée au dépôt et à la diffusion de documents scientifiques de niveau recherche, publiés ou non, émanant des établissements d'enseignement et de recherche français ou étrangers, des laboratoires publics ou privés.

Fatigue properties of as-built and heat-treated Inconel 625 obtained by the hybridization of two laser-powder based additive processes

Noémie Martin^{a,b,*}, Anis Hor^a, Etienne Copin^a, Philippe Lours^a, Léon Ratsifandrihana^b

^a Institut Clément Ader (ICA), Université de Toulouse, CNRS, IMT Mines Albi, INSA, ISAE-SUPAERO, UPS, 3 rue Caroline Aigle, 31400 Toulouse, France

^b SEGULA Engineering, Immeuble EQUINOX - Bâtiment I, 24 Boulevard Déodat de Séverac, 31770 COLOMIERS, France

Laser Powder Bed Fusion and Direct Energy Deposition processes have complementary characteristics. Their hybridization can increase the variety of applications for additive manufacturing. This paper investigates the static and fatigue behaviors of hybrid Inconel 625 parts using monotonic and high cycle fatigue tests, local strain measurements and self-heating method. Fatigue properties of as-built and recrystallized LPBF, DED and hybrid Inconel 625 were evaluated and compared. The effect of heat treatment on hybrid microstructure homogeneity was investigated. Their consequences on mechanical compatibility and fatigue strength were proved. The fatigue strength was attributed to the competition between defects and the strain compatibilities.

1. Introduction

The growing interest in metallic additive manufacturing is usually related to the design freedom and the gain in time between the design and the production of the parts [1–4]. Initially used for prototyping [5,6], metallic AM is now common for structural repair and high value parts manufacturing, especially in aeronautics and medical domains [7]. Nickel-based superalloys are commonly used in aeronautical engines, for example for blade applications, because of their outstanding mechanical strength at high temperatures. Engine blades are subject to constant innovation in terms of geometry and function integration (such as cooling ducts) and hence stand as a promising application for AM [8]. The feasibility of such specific geometries, and the behavior of such alloys made by AM is therefore of great interest.

Several metallic AM technologies have been developed, differentiated by the type of raw material used (powder, wire), the physical principle (fusion, sintering) or the energy source (laser, electric arc, electron beam). Each technological choice leads to specific parts characteristics [9]. The comparison of AM technologies has a clear industrial interest. Among the various existing technologies, Laser Powder Bed Fusion (LPBF) and Direct Energy Deposition (DED) are based on the fusion of metallic powder using laser energy. LPBF benefits from a good process maturity, leading to an outstanding geometrical resolution and good material soundness [10,11]. However, its production rate is limited, and its running costs relatively high [7]. DED has a better

production rate, and a great flexibility. The deposition can be performed on any substrate shape. Literature already accounts for attempts to exploit the complementarity between the two processes [8,12,13]. These industrial proofs of concept highlight the potential of AM hybridization, but also identified challenges in process control and material reliability. The satisfactory mechanical resistance of hybrid parts still requires to be demonstrated.

Indeed, Jones et al. observed pores, cracks, and a Heat Affected Zone (HAZ) at the interface between the DED deposit and the substrate [3]. The impact of such interface on the tensile behavior was also investigated for various hybrid configurations: interface at 90° [14], 45° [12] or 0° [15] relative to the solicitation direction. The mechanical strength of this interface was also analyzed in the case of recharging process [16]. Under monotonic tensile loading, the failure occurs mostly in the DED microstructures [17,18]. One exception in literature would be DED-casting hybridization [19], for which the tensile strength of the coarse microstructure induced by casting is weaker than that of the DED microstructure.

In the case of LPBF-DED hybridization, the microstructures induced in both sections are highly dependent on process parameters [20–22], but literature generally agrees that the LPBF process induces a finer microstructure and a higher mechanical strength than the DED process does. Marchese et al. compared Inconel 625 obtained by LPBF and DED, and confirmed that LPBF Inconel 625 shows a finer microstructure leading to higher hardness [20]. The rare publications concerning LPBF-DED hybridization focus on the technological feasibility [23,24], but

Nomenclature

AB	As-built
AM	Additive Manufacturing
DED	Directed Energy Deposition
EBSD	Electron Backscatter Diffraction
HAZ	Heat Affected Zone
HT	Heat-treated
IPF	Inverse Pole Figure
LoF	Lack of Fusion
LPBF	Laser Powder Bed Deposition
SEM	Scanning Electronic Microscope
UTS	Ultimate Tensile Strength
YTS	Yield Tensile Strength
Nf	Number of cycles to failure
ϵ_{moy}	Mean global strain during tensile testing
σ_{max}	Maximal stress for a cyclic loading

some propose a characterization of the impact of the interface as well as the microstructural heterogeneity on the mechanical strength. Li et al. produced hybrid LPBF-DED Ti-6Al-4V samples and showed that, despite a HAZ reaching several millimeters of depth and a heterogeneous microstructure, the metallurgical bonding at the interface was satisfactory [25]. During the tensile loading, the failure occurred systematically in the DED deposit, between two layers. These conclusions were supported by the in-situ SEM tensile observations on the Inconel 718 wrought substrate and DED deposit presented by Guévenoux et al. [26], attributing the strain localization at the DED inter-layer to the Hall-Petch effect and to the suspected presence of small defects and discontinuities [26]. Qin et al. confirmed that for a LPBF-DED Ti-6Al-4V hybrid parts, the DED microstructure was the limiting factor for tensile strength even after a heat treatment [14]. Oh et al. showed that the depth and geometry of the notch in the case of the repair of a 316L steel part has an impact on the interface soundness [15]. They observed a HAZ, as well as cracks or pores between the substrate and the deposit which were considered responsible for the tensile failure.

More recently, Godec et al. analyzed the tensile behavior of hybrid LPBF-DED Inconel 718 samples [12]. The authors observed a fine microstructure with a high dislocation density in the LPBF section, while the DED microstructure displayed large columnar grains with occasional fine equiaxial zones. The resulting difference in mechanical properties between the LPBF and DED Inconel 718 was identified as a limitation for hybridization. A homogenizing heat treatment was applied on the hybrid parts, but the DED section was not entirely recrystallized and undesirable secondary phases were observed. As for the previous studies on Ti-6Al-4V, the failure systematically occurred in the DED section for as-built and heat-treated hybrid samples. Optical measurements showed that the strain is concentrated in the DED section. This strain localization has been shown to be the cause of the decrease in tensile elongation as well as responsible for the difference of monotonous tensile behavior between a mono-process part and a hybrid part [27].

Thereby, the monotonous tensile behavior of hybrid parts is relatively well documented in the literature, but the fatigue behavior of such parts is still very scarcely studied. Balit et al. investigated the axial fa-tigue properties of 316L stainless steel parts made by hybridization of a wrought substrate and a DED deposit [18]. Using the self-heating technique, they established that the fatigue properties of hybrid parts are not as good as for the mono-process parts. However, they did not clearly show the impact of the hybridization, particularly that of the interface on the fatigue strength, and the deterioration of properties has not yet been explained.

The objective of this paper is to investigate the mechanical strength of hybrid LPBF-DED Inconel 625 samples both under static and fatigue

loading. The role of the interface and the impact of the microstructural heterogeneity is studied experimentally. The local strain fields are quantified during static and cyclic solicitations and linked with the fa-tigue strength. As-built and heat-treated microstructures are compared, which allows further analysis of the role of microstructure, and sets original perspectives for industrial applications.

2. Materials and methods

2.1. Inconel 625 powders

The powders were chosen according to the machine manufacturer's recommendations. The LPBF powder was supplied by *SLM Solution*, and the DED powder by *Höganäs*. Table 1 details their granulometry and chemical composition as given by the suppliers.

Additional LPBF samples were printed using the Höganäs powder to check for a possible impact of the powder. LPBF samples obtained using Höganäs and SLM Solution powders both showed identical metallurgical and mechanical properties. In the following, the powder's impact will be neglected. The differences between LPBF and DED parts will therefore be attributed to the manufacturing process.

2.2. LPBF, DED and hybrid processes

All samples were printed vertically by LPBF, DED or both processes for hybridization. The LPBF samples were built as near-net-shape using a SLM Solution 125HL machine. The DED samples were built as cylinders using a BeAM Modulo 500 machine, and then machined to the final geometry. The recommended optimized process parameters were used (given on Table 2).

The hybrid samples were built in two steps using the same LPBF and DED equipment and parameters. First, vertical cylinders with 12 mm diameters and 50 mm height were built by LPBF. Then, they were completed by DED directly on the top LPBF layer, up to a height of 100 mm (Fig. 1).

2.3. Reference materials: as-built and heat treated Inconel 625

A good metallurgical bonding is observed between the LPBF substrate and the DED deposit (Fig. 3a), with only occasional entrapped gas pores, observed in mono-process samples as well. At the interface, rare lacks of fusion (Fig. 2b) are observed. The microstructure of the LPBF substrate remains identical to a LPBF-only sample, with dendritic structures and chemical micro-segregations of the heavy alloying elements Nb and Mo. The first layers of the DED deposit display a slightly finer microstructure than that of mono-DED samples, with fine columnar grains. After several millimeters, the large columnar grains and high crystallographic texture typical of the DED microstructure obtained by the chosen parameters are observed (Fig. 3a). In comparison, the LPBF microstructure is fine with a low level of texture and is homogeneous throughout the sample.

A heat-treatment of 4 h at 1150 °C followed by a water-quench successfully recrystallized the microstructure and erased the chemical

Table 1
LPBF and DED powders' granulometry and chemical composition.

	Powder size (deciles)	Chemical composition (wt %)					
		Ni	Cr	Mo	Nb + Ta	Fe	Co
LPBF powder (SLM solution)	D ₁₀ = 21 µm	Bal.	21.41	8.99	3.69	4.13	0.16
	D ₅₀ = 34 µm						
	D ₉₀ = 54 µm						
DED powder (Höganäs)	D ₁₀ = 47 µm	Bal.	20.5	8.5	3.93	4.08	0.17
	D ₅₀ = 67 µm						
	D ₉₀ = 94 µm						

Table 2
LPBF and DED process parameters used for Inconel 625 samples.

Energetic Parameters			Strategy	
LPBF	Laser power	275 W	Hatch distance	0.12 mm
	Laser speed	760 mm/s	Hatch stripe length	10 mm
	Layer thickness	0.05 mm	Rotation layer to layer	67°
	Building plate temperature	200 °C		
DED	Laser power	900 W	Concentric circles from outer to inner circle	
	Laser speed	13 mm/s		
	Powder flow	9.5 g/min		
	Spot size	1.9 mm		
	Delay between layers	21 s		

heterogeneity (Fig. 3b). Both the DED deposit and the LPBF substrate display equiaxed grains, with a high density of twin boundaries, commonly observed in conventional nickel-based superalloys [28,29]. Both the heat-treated LPBF and DED Inconel 625 microstructures have similar fully recrystallized aspect, but a significant scale difference remains (Fig. 4b). The mean grain size of the heat-treated DED section is $121 \pm 90 \mu\text{m}$ while the heat-treated LPBF has an average grain size of $32 \pm 38 \mu\text{m}$.

The difference in microstructures of LPBF and DED Inconel 625 results in different mechanical properties. The induced specific monotonous behavior is detailed in a previous study [27], and the main properties of the as-built and heat-treated samples are recalled in the Table 3. The heat treatment reduces the gap in properties between LPBF and DED Inconel 625, which is beneficial to the monotonous behavior of

a hybrid part.

2.4. Test specimen geometries and elaboration

For the following study, three sample geometries were used depending on the mechanical test performed. Cylindrical samples of diameter 8 mm were used for the fatigue tests of the mono-process LPBF and DED, as-built and treated (Fig. 4.a1). Similar cylindrical samples, but with a thinner diameter of 5 mm were used for the fatigue tests of hybrid specimens, as-built and treated (Fig. 4.a2). Finally, flat specimens (Fig. 4.b) were used for the monotonic tests of hybrid samples as-built and treated, because this geometry allows for image correlation measurements.

The LPBF fatigue specimens were printed as near-net-shapes geometries. Some of them were then heat-treated. The DED fatigue specimens and Hybrid fatigue specimens were obtained by machining of as-built or treated raw cylinders (Fig. 1). All the cylindrical samples, near-net-shape and machined, were polished on a semi-automated set-up. The polishing set up is made of a rotative felt drill gently put in contact with the turning sample. The abrasive medium used are diamond suspensions, and the finest size used is $10 \mu\text{m}$. The obtained surface roughness is under $5 \mu\text{m}$, and has no influence on the fatigue behavior of the samples.

The flat samples were extracted from the raw hybrid cylinders by EDM to the geometry given in the Fig. 4.b. They were manually polished to remove the surface oxidation, and a speckle paint was applied on the surface.

2.5. Tensile tests conditions

Hybrid flat tensile samples (Fig. 4.b) were instrumented with an optical extensometer on the full gauge length, and speckle paint for

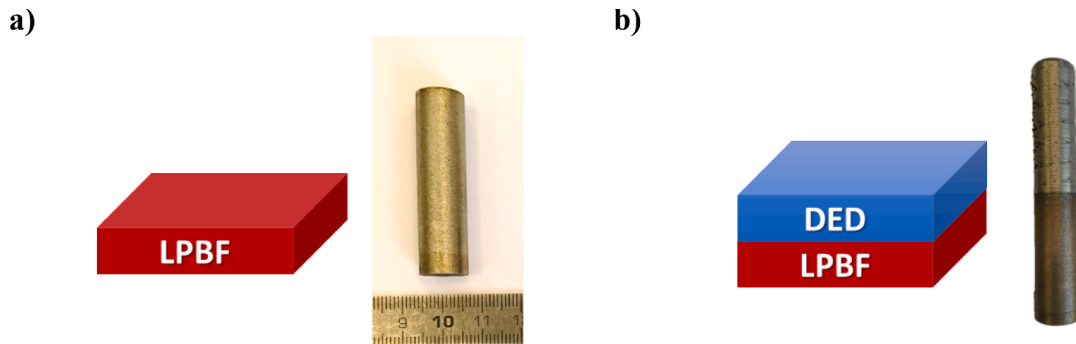


Fig. 1. The two fabrication steps for LPBF-DED hybrid samples: a) LPBF b) DED.

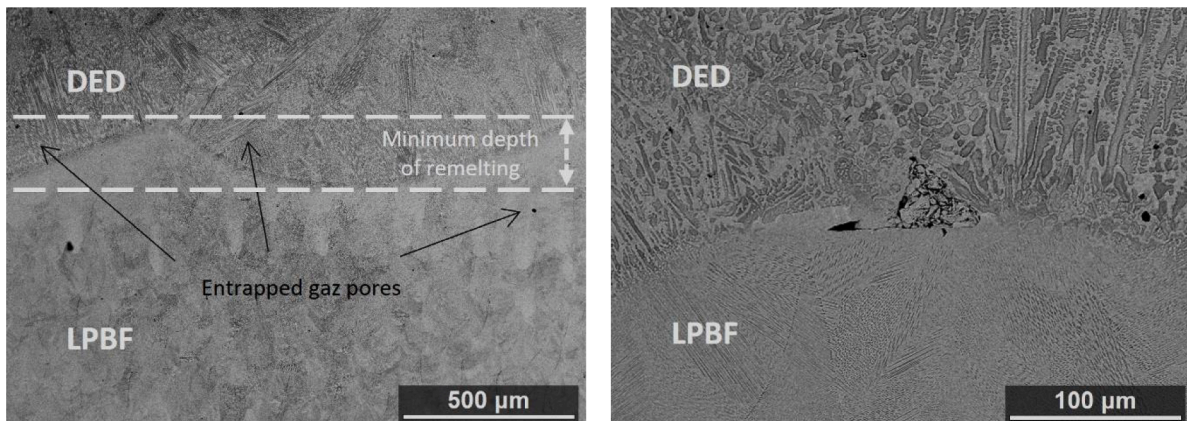


Fig. 2. SEM observations of the as-built hybrid microstructures in the vicinity of the LPBF-DED interface.

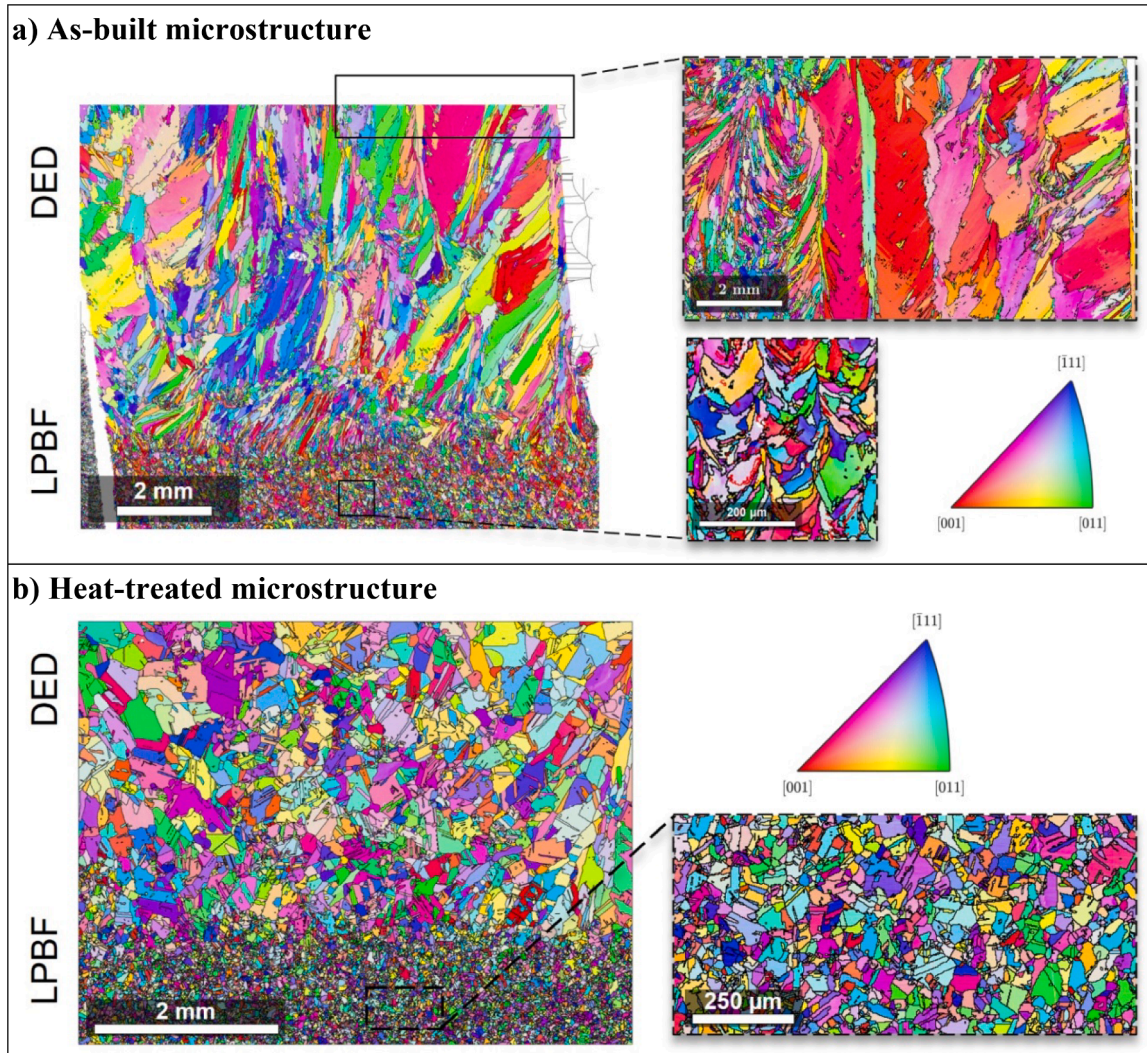


Fig. 3. Z-axis IPF EBSD maps of a) as-built b) heat treated hybrid LPBF-DED Inconel 625 in the vicinity of the interface.

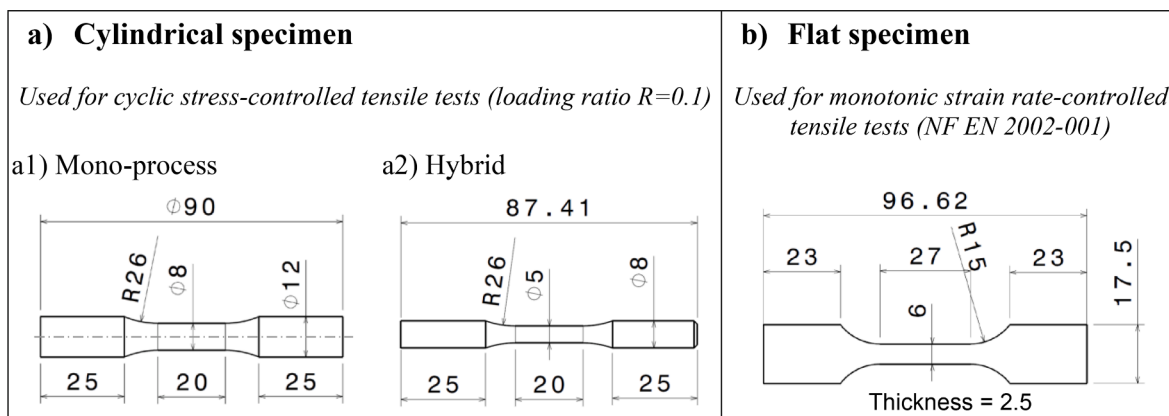


Fig. 4. Geometries of the a) cylindrical and b) flat specimens, dimensions in [mm].

digital image correlation (DIC) analysis [27]. The strain rate-controlled tests were conducted using the optical extensometer. According to the NF EN 2002-001 standard, two strain rates were used: $8 \times 10^{-5} \text{ s}^{-1}$ until 0.5% strain, and $1.5 \times 10^{-3} \text{ s}^{-1}$ until failure. Images were recorded throughout the test with two cameras at an acquisition frequency of 2 Hz. The strain fields were computed using VIC3D software.

2.6. Fatigue tests conditions

All fatigue investigations were carried out on a MTS 810 machine, using cylindrical samples (Fig. 4.a). The tests were stress-controlled, with a load ratio of $R = 0.1$ and a frequency of 15 Hz. In the following, the load levels are expressed using the maximal stress σ_{\max} to

Table 3

Mechanical and microstructural properties of as-built and heat-treated Inconel 625 obtained by LPBF and DED [27].

		YTS (MPa)	UTS (MPa)	Elongation (%)	Microhardness (HV _{300g})	Grain size $\bar{D}_{eq} \pm \sigma/2$ (μm)	Density (%)
LPBF	AB	667 ± 3	939 ± 1	39 ± 2	290 ± 4	11 ± 7	>99.9%
	HT	363 ± 4	853 ± 6	62 ± 2	218 ± 3	33 ± 15	
DED	AB	433 ± 12	779 ± 6	56 ± 2	230 ± 6	32 ± 38	
	HT	360 ± 14	768 ± 1	73 ± 2	205 ± 5	121 ± 90	

facilitate the comparison between the loading and the elastic domain [30,31]. One can easily convert σ_{max} into the conventional alternating stress σ_a by applying a multiplying factor of 0.45.

• Local strains monitoring on hybrid samples

The hybrid samples were equipped with adhesive local strain gauges in the LPBF and DED sections. The samples were solicited for 3000 cycles at load levels σ_{max} between 100 and 700 MPa. The local strains of hybrid samples were recorded and compared to the global stress-strain response of the samples.

• High cycle fatigue tests up-to-failure

Other samples were solicited at a constant load level up-to failure. The S-N diagram was plotted for as-built and heat-treated samples batches (LPBF, DED and hybrid). If the sample reached the conventional fatigue life of $2.2 \cdot 10^6$ cycles without failure, the test was stopped. Subsequently, SEM observations were performed on the fracture surface to investigate the crack initiation and propagation mechanisms.

• Self-heating method

The high cycle fatigue limit was investigated using the self-heating method, which is based on the microplasticity mechanisms, detected through thermal energy dissipation [32–35]. Fig. 5 illustrates one sample mounted and ready to be tested. The samples used for the self-heating tests were instrumented with two thermocouples each. On the mono-process samples, one thermocouple was positioned in the middle of the sample, and one other at one third of the gauge length. The change in temperature measured in both thermocouples were similar. For hybrid samples, one thermocouple was in the middle of the LPBF section, and a second one in the middle of the DED section.

Two additional thermocouples were also positioned on the grips to monitor the evolution of their temperature. The samples were loaded at different stress levels for 3000 to 5000 cycles until their temperature

stabilized (Fig. 5). The sample was left to cool down between two solicitations.

The temperature ΔT is computed for each stress level, using the following equation [36,37]:

$$\Delta T = (T_f - T_0) - \frac{(T_{uf} + T_{lf}) - (T_{u0} + T_{l0})}{2} \quad (1)$$

where T_f is the stabilized temperature at the surface of the specimen, T_0 is the initial temperature at the surface of the specimen, T_{l0} and T_{u0} the initial temperatures of the upper and lower grips, and finally T_{lf} and T_{uf} are the final lower and upper grip temperatures. For all tests performed, the temperature of the upper and lower grips did not change. Equation (1) is therefore reduced to:

$$\Delta T = T_f - T_0 \quad (2)$$

The temperatures ΔT are plotted as a function of the corresponding applied maximum stresses to determine the primary and secondary regimes (Fig. 6) [38]. The intersection of the two regimes is used to identify graphically the fatigue limit. Several identification techniques are reported in the literature: (i) the intersection of the two asymptotes on Cartesian or logarithmic [32,37] plots were traditionally used, (ii) the first significant temperature raise and slope of temperature change [39], (iii) the development of numerical models to further understand and characterize this technique [34,35]. In this study, the first method is used. It assumes that fatigue failure results from plastic strain accumulation mechanisms and is theoretically demonstrated [40]. In this method, the first raises in temperature is considered as transition between the two asymptotic regimes. The fatigue strength is identified at the abscissa of the intersection of the two asymptotes.

3. Experimental results

3.1. Heterogeneous response of hybrid samples to monotonic and cyclic loading

The difference of microstructure between Inconel 625 made by LPBF

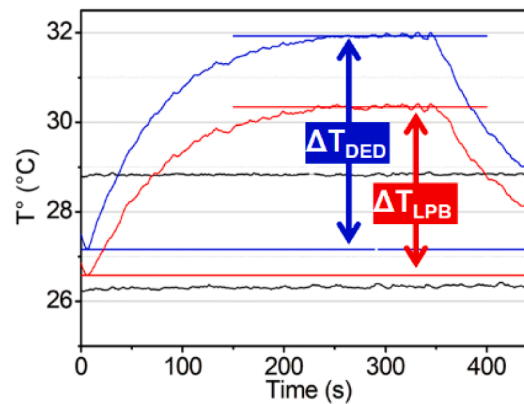
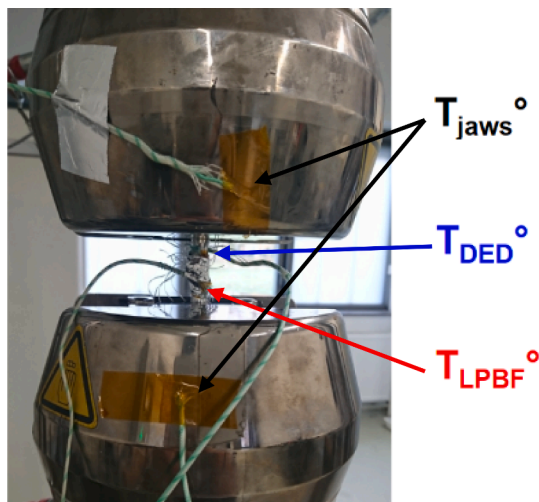


Fig. 5. Illustration of the self-heating set-up and example of temperature measurement.

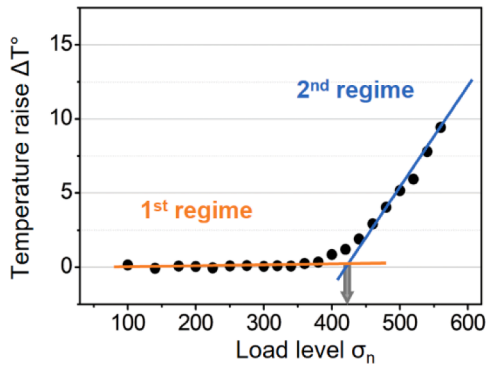


Fig. 6. Example of a temperature raise versus load level plot obtained and determination of fatigue limit.

and by DED causes heterogeneous mechanical behavior of hybrid samples under tensile tests [27]. The recrystallisation achieved by the heat treatment reduces the gap in properties but does not erase the difference. In both cases, the failure occurs in the DED section, which has a lower yield resistance than the LPBF.

Further investigation of the strain fields during the monotonic test is presented in Fig. 7 for as-built and heat-treated samples respectively. The strain along the median line of the sample is plotted for each frame during the tensile test. The color of the plotted line indicates the

corresponding global strain of the sample measured by the optical extensometer.

The color scale bar is not linear because of the change of strain-rate during the tensile test. Two strain rates were applied according to the NF EN 2002-001 standard: $8 \times 10^{-5} \text{ s}^{-1}$ until 0.5% strain, and then $1.5 \times 10^{-3} \text{ s}^{-1}$ until failure. Images were recorded throughout the test with two cameras at 2 Hz acquisition frequency. Hence at the beginning of the test, the slow strain-rate allows for pictures in a lower deformation range than at the end of the test when the strain rate is increased.

For all samples, the localization of the strain in the DED section is obvious for global strains exceeding 0.2 %. This heterogeneity of behavior is even more significant in the case of as-built samples, where the deformation of the DED section exceeds 15 %, whereas the global deformation barely reaches 5 %. Simultaneously, less than 2 % strain is reached in the LPBF section.

After heat-treatment, the heterogeneity is still observed, but to a lesser extent with a maximal strain of 10 % in the DED and more than 4 % in the LPBF section for a global strain of 5 %.

Furthermore, the focus on low global strains given in Fig. 7a.ii and b. ii reveal that the strain localization in the DED section only starts when the global strain exceeds 0.2 %. For global strain levels below 0.2 %, the behavior of LPBF-DED hybrid samples is homogeneous.

Fig. 8 shows the behavior of hybrid samples under cyclic stress-controlled loading. All cyclic tests are performed with a minimum stress to maximum stress ratio of 0.1. The strain-stress evolution of the LPBF section (in red) and the DED section (in blue) are plotted for 3000

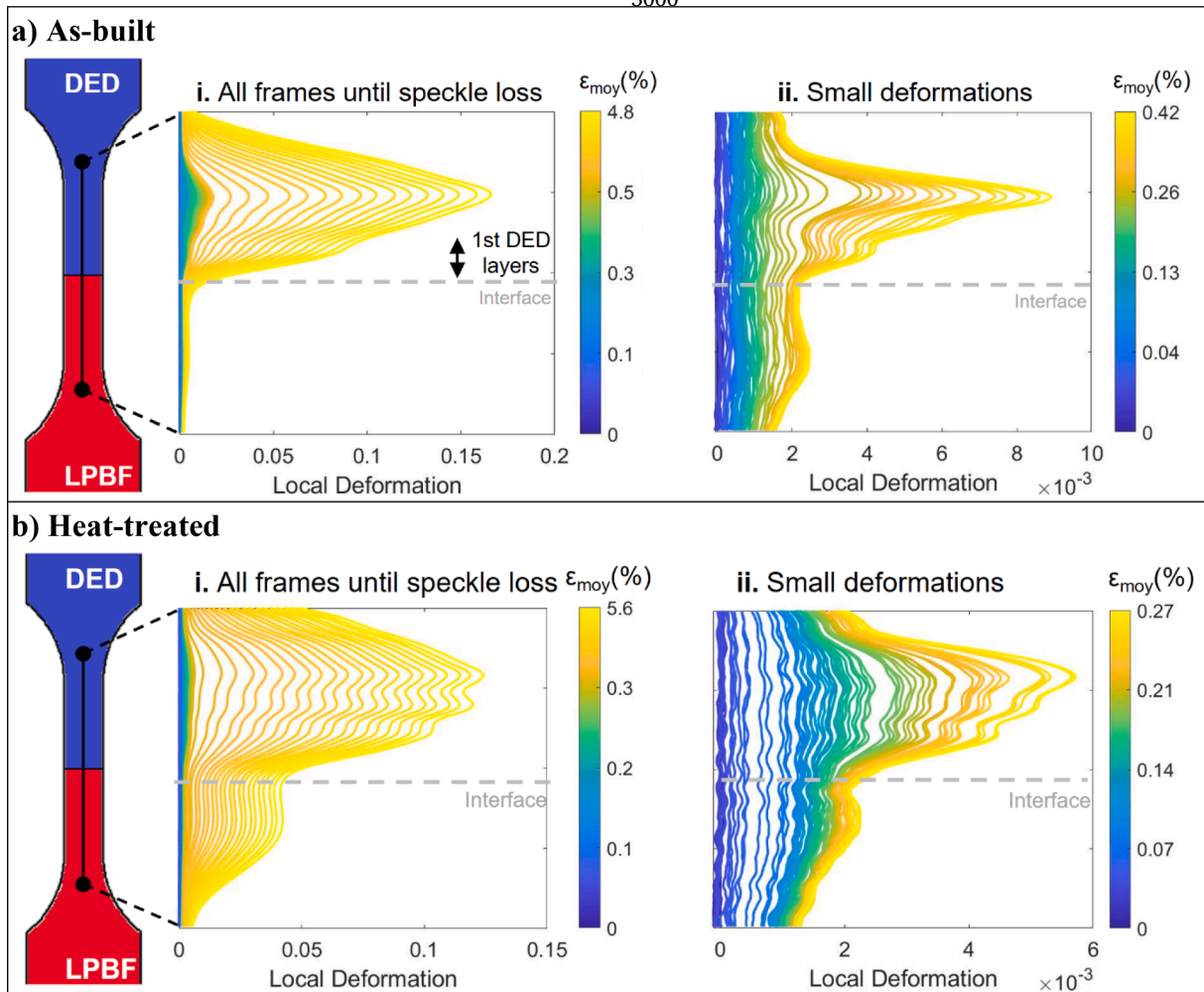


Fig. 7. Evolution of the local strain profile along the a) as-built and b) heat-treated hybrid samples during tensile test. The color scales give the global elongation measured by the optical extensometer i. until speckle loss, ii. for small deformations.

cycles at various load cases ($\sigma_{\max} = 300, 400$ and 500 MPa). The loads investigated are both lower and higher than the yield stress of DED (AB 433 MPa; HT 360 MPa) and LPBF (AB 667 MPa; HT 363 MPa) Inconel 625.

The case of loading between $\sigma_{\min} = 30$ MPa and $\sigma_{\max} = 300$ MPa (Fig. 8a1, b1) is under the yield tensile stress of LPBF as-built (45% of YTS), DED as-built (69%) and LPBF heat-treated (83%), DED heat treated (83%). And indeed, as-built and heat treated hybrid samples display a quasi-elastic cyclic response in both LPBF and DED sections. A slight plastic strain accumulation of about $+0.02\%$ is observed on the as-built sample, but not after the heat treatment. The as-built micro-structure of LPBF and DED Inconel 625 is heterogeneous with a high dislocation density. This specific microstructure causes local variations in mechanical properties, and therefore plastic strains localization [26]. After the heat treatments, these heterogeneities are erased.

For higher loading cases (Fig. 8a2, b2 and a3, b3), both LPBF and DED sections are subject to elastic shakedown phenomena. However, the residual deformation of the LPBF section is lower than that of the DED section. For the loading at $\sigma_{\max} = 400$ MPa, the mean strain of the DED section increases by $+0.5\%$, versus less than $+0.15\%$ for the LPBF section. After heat treatment, the gap is reduced with $+0.45\%$ for the DED and $+0.2\%$ for the LPBF. For the loading at $\sigma_{\max} = 500$ MPa, the strain gauges suffered adhesive failure, preventing from quantifying the gap between the responses of the LPBF and DED sections, but it is clearly worsening. The as-built LPBF stabilizes under $+1\%$ mean strain, while the DED exceeds $+3\%$, with up to $+0.2\%$ strain accumulation per cycle at the beginning of the fatigue test. After heat treatment, the DED

stabilizes at a smaller strain level, but it remains greater than the LPBF's.

Finally, the Young modulus of LPBF and DED Inconel 625 were different. The Young modulus observed on the LPBF sections of the samples is approximately 210 GPa, versus approximately 150 GPa for the DED in both states, as-built and treated. It must be emphasized here that these tests do not permit a reliable measurement of the Young modulus. The samples are hybrid samples, with highly heterogeneous properties, and can be considered as structures. Nevertheless, inferior modulus of the as-built DED could be explained by the significant crystallographic texture [41]. However, the difference remains after the recrystallization by heat treatment, which rules out texture as the only cause for this difference.

3.2. High cycle fatigue behavior

The S-N plots obtained by stress-controlled cyclic tests with a stress ratio $R = 0.1$ are given in Fig. 9a, for the as-built samples, and Fig. 9b, for heat-treated samples. For the higher stress levels, all samples display similar fatigue strength. However, the LPBF as-built samples show lower fatigue strength at $2.2 \cdot 10^6$ cycles compared to DED and hybrid samples. After the heat treatment, all six batches (as-built and heat-treated, LPBF, DED and hybrid) reveal a lower scattering dispersion for all load levels and similar fatigue resistance at $2.2 \cdot 10^6$ cycles. The significant improvement of LPBF fatigue strength due to heat-treatment is already documented in another paper and attributed to the significant improvement in microstructure ductility [30].

In the case of DED and hybrid samples, the fatigue strength is not

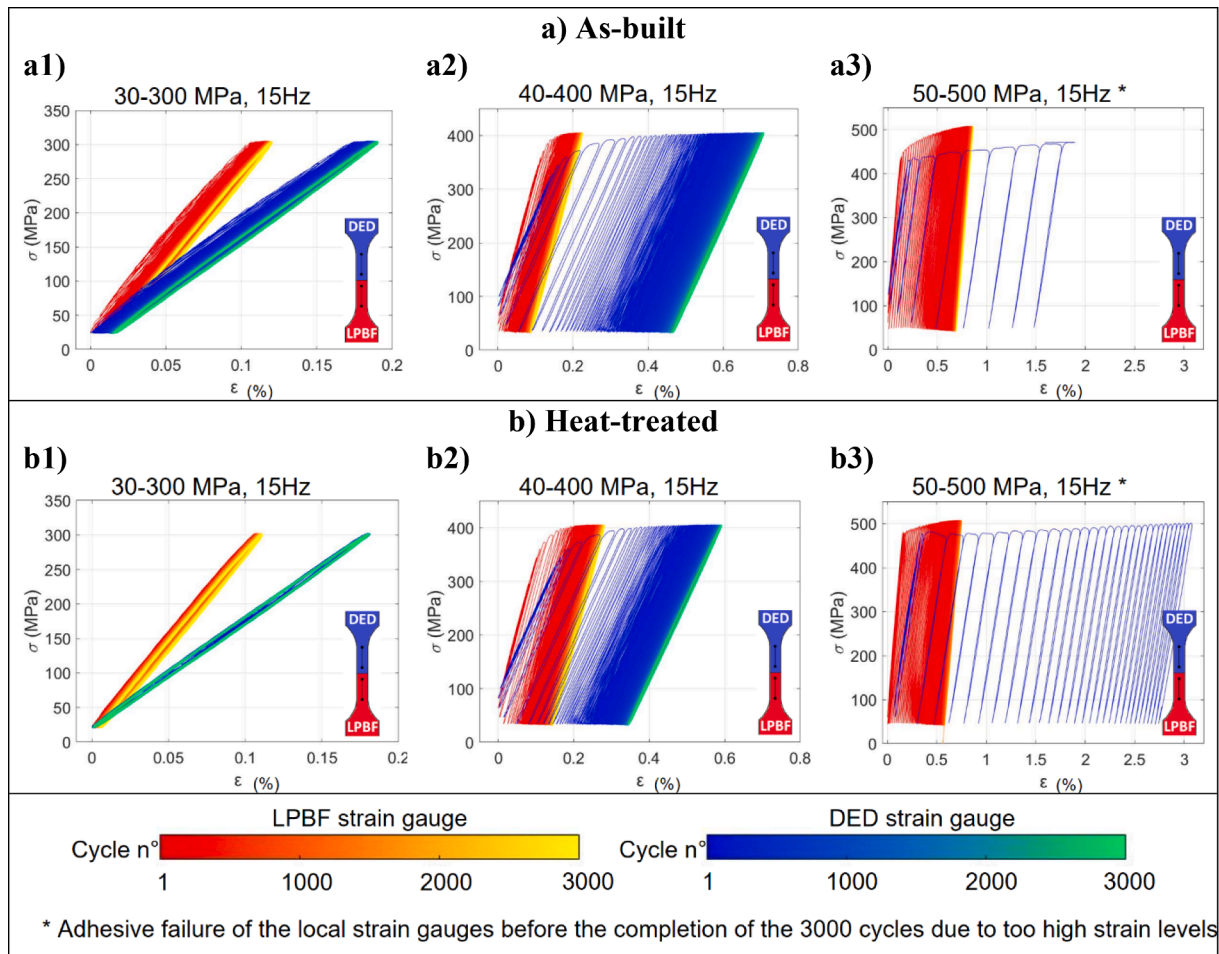


Fig. 8. Stress-strain response of the LPBF (red) and DED (blue) sections of a) as-built and b) heat-treated hybrid samples for different alternative stress levels. (For interpretation of the references to color in this figure legend, the reader is referred to the web version of this article.)

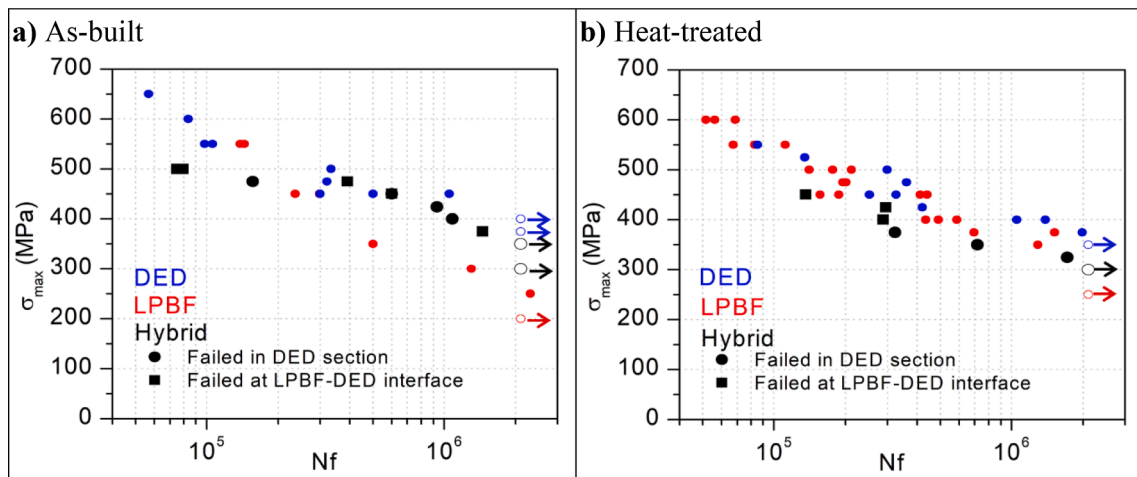
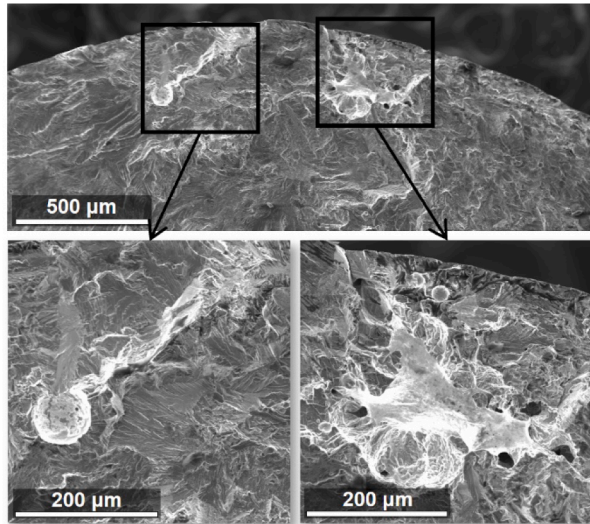


Fig. 9. S-N plots for a) as-built and b) heat-treated LPBF (red), DED (blue) and hybrid (black) samples tested up-to-failure. Empty markers represent non-broken samples stopped at $2.2 \cdot 10^6$ cycles. (For interpretation of the references to color in this figure legend, the reader is referred to the web version of this article.)

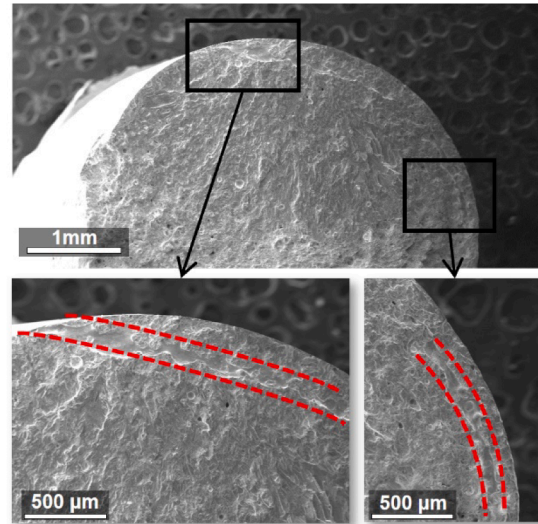
notably impacted by the heat treatment. The tendency and order of magnitude of fatigue strength are similar between Fig. 9a and Fig. 9b, despite the evolution in monotonic behavior and properties detailed previously. The decreases in yield tensile stress of LPBF, DED and hybrid heat-treated samples do not alter the fatigue strengths, nor improve it significantly.

Fig. 9 also shows that the hybrid samples, both as-built and heat-treated, systematically fail in the DED section, or at the interface. As illustrated by the low dispersion scattering in Fig. 9, the fatigue strength is independent on the fracture localization in both case: hybrid as-built and hybrid heat treated. Moreover, no trend is identified between the loading level and these failure localizations.

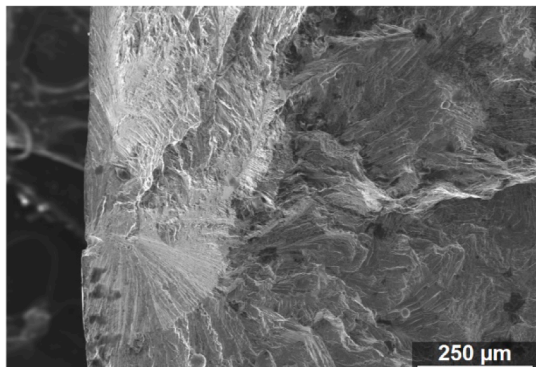
a) Hybrid sample, failed in DED section



b) Hybrid sample, failed at interface



c) DED sample, failed on microstructure



d) LPBF sample, failed on LoF

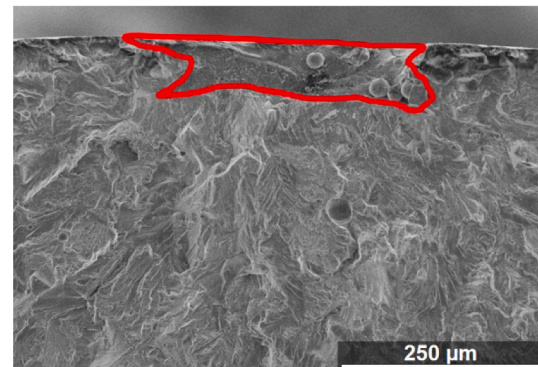


Fig. 10. Fractographic SEM images of representative failures of as-built a-b) hybrid, c) DED, d) LPBF samples.

3.3. Failure analysis

The fatigue failures were investigated by SEM. The analysis revealed the presence of defects at all initiation sites for LPBF and hybrid samples. These defects are systematically located on or near the surface of the samples. In the DED samples, the crack initiated on the microstructure. The initiation mechanisms were identical for as-built and heat-treated samples which may explain the small difference between the two states (as-built and heat-treated). Only the as-built samples are illustrated in Fig. 10.

In hybrid samples failed in the DED section, defects were systematically observed at the crack initiation sites (Fig. 10a). The irregular shape of these defects allows to link them to fluid movements of the melt pool, commonly described as “Marangoni defects” [42]. This type of defects was unexpected as none had been observed in the mono-process DED samples obtained with the same process parameters.

All cracks that initiated at the interface between the DED deposit and the LPBF substrate on hybrid samples revealed a circular lack of fusion (Fig. 10b). Its dimension and consistency recall the circular lasing strategy used for the DED deposit (Table 2). The first layers are deposited on substrate at a room-temperature, and the bonding between DED melting pools is not regular in comparison to higher layers because the steady state is not yet established.

To conclude, the initiation sites observed on the hybrid samples were different than that of the mono-processes samples. On the one hand, the DED samples, as-built or treated, revealed systematic fracture initiation on microstructure without identifiable defects (Fig. 10c). On the other hand, one or several lacks of fusion defects were identified at the initiation site in each LPBF sample (Fig. 10d).

The Fig. 11 shows the two main propagation mechanisms observed in all samples: crystallographic failure around the initiation site, for small crack size, followed by ductile failure, easily noticeable by the fatigue striations [30].

3.4. High cycle fatigue strength evaluated by self-heating method

The self-heating results are presented in Fig. 12a for the mono-process as-built samples and in Fig. 12b for the mono-process heat-treated samples. The temperature raises are plotted versus the applied stress levels of LPBF (red) and DED (blue) samples.

The LPBF and DED self-heating curves present a difference in the transition between the two regimes’ asymptotes. In the case of DED

samples, the temperature increases are close to the asymptotes for all loads levels. In the case of LPBF samples, the temperature raises in the vicinity of the transition is higher than the asymptotes. Furthermore, in the case of as-built LPBF (Fig. 12a), the sample failed following the 2000 first cycles at σ_{max} 700 MPa. Hence it is suspected that the second regime is not yet fully reached, and the resulting intersection is slightly underestimated, and that the transition is even farther from the asymptotes.

Nevertheless, Fig. 12a shows that the self-heating fatigue limit of the as-built LPBF (600 MPa) samples was significantly higher than the DED as-built samples (450 MPa). After the recrystallization by heat treatment, the gap between the two microstructures was drastically reduced, with 450 MPa for LPBF samples and 400 MPa for DED samples. The limits found by the asymptotes are significantly superior to those found by the S-N curves. This difference could be caused by the presence of defects, not taken in account in the asymptote analysis.

Contrary to the measurements performed on mono-process samples where self-heating curves are computed separately on different specimens, the two self-heating fatigue curves of hybrid samples are obtained from a single specimen by positioning two thermocouples: the first in the LPBF section and the second in the DED section. The measurements performed on these hybrid samples are illustrated in Fig. 12a for the as-built state and in Fig. 12b for the heat-treated state. The empty symbols represent the previous measurements on the LPBF and DED mono-process samples. Filled symbols represent each section of the hybrid samples (red for LPBF and blue for DED). Likewise mono-process samples, the LPBF section displayed a fatigue limit slightly higher than the DED section. However, the difference between the LPBF and DED sections was significantly lower than that between the mono-process LPBF and DED samples. The heat transfers between the LPBF section and the DED section in hybrid samples may explain this decrease. In the case of heat-treated samples, a given load case caused a lower global increase in temperature of hybrid samples compared to that of mono-process samples. This can be explained by the difference in sample geometry. The hybrid samples have a smaller diameter and hence exhibit less energy dissipation. However, because the asymptotes intersection is used and not the absolute temperature increase, the results remain comparable.

As-built hybrid samples (Fig. 13a) displayed a fatigue limit slightly superior to 450 MPa for the DED section, which was similar to the limit identified on DED mono-process as-built samples. The LPBF section shows a slightly better fatigue limit, above 500 MPa, but this limit was significantly lower than the 600 MPa limit identified on LPBF samples.

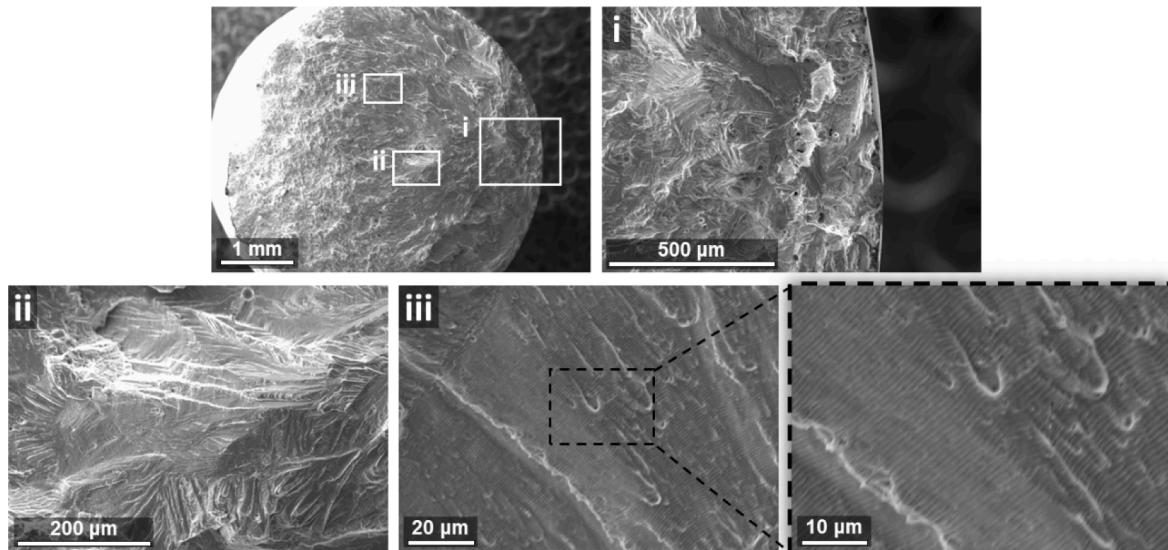


Fig. 11. Fractographic SEM images of a hybrid fatigue sample failed in the DED section. i. Initiation site, ii. Crystallographic failure, iii. Ductile failure and fatigue striations.

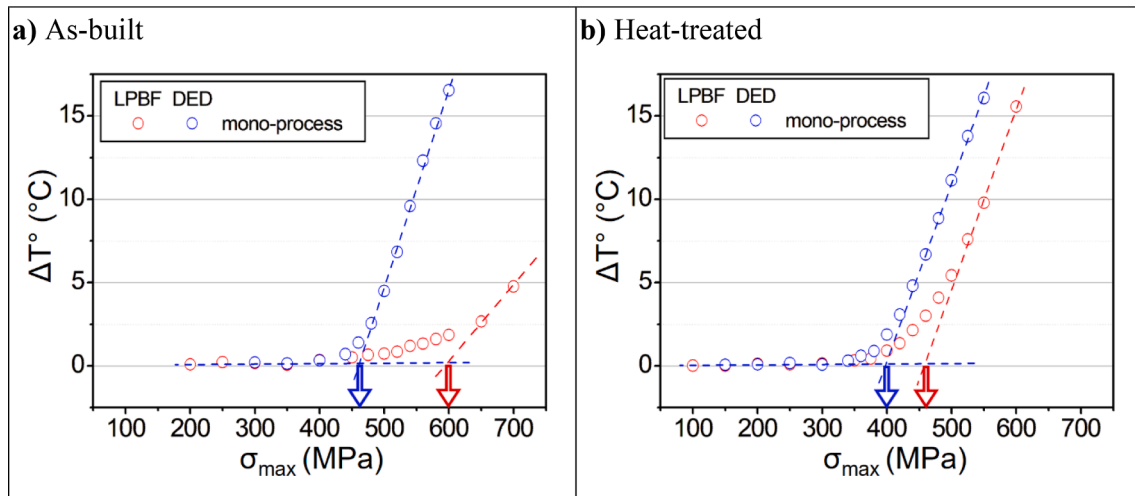


Fig. 12. Self-heating fatigue curves for a) as-built, and, b) heat treated LPBF (red) and DED (blue) mono-process samples: self-heating temperatures as a function of their corresponding maximum stress levels. (For interpretation of the references to color in this figure legend, the reader is referred to the web version of this article.)

After heat treatment, all limits identified were in the range 400–450 MPa (Fig. 13.b), whether it was measured on LPBF, DED, hybrid or mono-process.

Finally, Table 4 summarizes experimental yield tensile stresses (YTS) and fatigue strengths estimated from S-N curves and from self-heating curves. The fatigue strengths estimated from S-N plots are lower than the theoretical fatigue limits identified from self-heating method. This difference is particularly significant for LPBF samples, as well as as-built DED samples.

4. Analysis and discussion

4.1. Impact of defects and damage initiation on fatigue strength

The simultaneous analysis of S-N plots and fractographic study of the tested samples can highlight the impacts of defects on the fatigue behavior of samples [43,44]. For the low stress levels, the crack initiation phase, highly impacted by defects, is preponderant in fatigue life as compared to the propagation [45]. The fatigue strength at $2.2 \cdot 10^6$ cycles of as-built LPBF is found to be 250 MPa versus 350 MPa after heat treatment. This improvement is even more significant considering the difference in the yield tensile stress between the as-built and the heat treated state. In the S-N plots illustrated in Fig. 13, the maximum stress

Table 4

Summary of Yield Tensile stresses and fatigue properties for LPBF, DED and hybrid Inconel 625 (as-built and heat treated).

		YTS	Fatigue strength determined	
			from S-N curves	from self-heating curves
LPBF	As-built	667 MPa	250 MPa	600 MPa
	Heat-treated	363 MPa	350 MPa	450 MPa
DED	As-built	433 MPa	400 MPa	450 MPa
	Heat-treated	360 MPa	400 MPa	400 MPa

was normalized by the yield tensile stress. As-built LPBF samples displayed fatigue strength, expressed in terms of maximum stress, lower than 50 % of its YTS, whereas after the heat treatment it can withstand a load case of more than 90 % of its YTS. The improvement was mainly attributed to the higher defect tolerance in the recrystallized and homogenized microstructure compared to the as-built microstructure [30].

Fig. 14b shows that the DED samples displayed fatigue strength at $2.2 \cdot 10^6$ cycles close to 100 % of their YTS, whether they were as-built or heat treated. Unlike the LPBF samples which were printed near-net-shape and polished, the DED samples were machined and then polished. The fractographic analysis of the samples confirmed that defects were systematically observed on the initiation sites for the LPBF

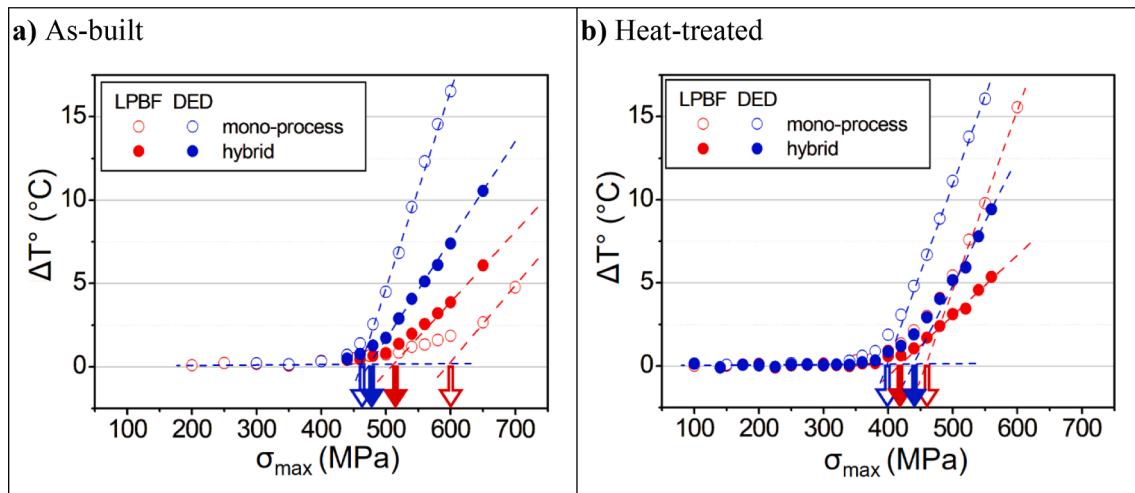


Fig. 13. Temperature raises of LPBF and DED sections of hybrid samples (full markers) and mono-process samples (empty markers), a) as-built b) heat-treated.

samples, while the DED samples mostly showed initiation sites within the bulk microstructure (Fig. 10b). The lack of surface defects is sufficient to improve the fatigue resistance of as-built DED Inconel 625 microstructure despite its heterogeneity and high dislocation density. This dislocation density is even higher in the case of LPBF samples and is assumed to be responsible for the low damage tolerance of this micro-structure [30].

According to these results on as-built mono-process samples, the hybrid samples should fail in the LPBF section, or at the interface. Yet, all the hybrid samples tested up-to-failure broke in the DED section or at the LPBF-DED interface (Fig. 9). The hybrid samples were machined and polished, unlike LPBF samples that were printed as near-net-shapes and just polished. LPBF is known to induce most defects around the surface of the samples [45]. Machining has removed this specific zone and the microstructure of the LPBF section in hybrid samples is believed to be almost free of defects. Hence, considering the results from self-heating, the fatigue strength of defect-free LPBF is superior to DED Inconel 625, which is consistent with the failures of hybrid samples taking place in the DED section.

This major impact of surface defects is also supported by a short review of the fatigue properties of Inconel 625 reported in the literature [46–51]. S-N plots issued from various fabrication processes are given in Fig. 15 (red for as-built LPBF, blue for as-built DED, black for wrought and grey for cast microstructures). The empty symbols correspond to results obtained with symmetric alternating loading ($R = -1$), and full markers are for conditions identical to this study's ($R = 0.1$). The fatigue strengths are represented in terms of maximal stress σ_{max} in Fig. 15a, and σ_{max} normalized by the respective YTS of each study in Fig. 15b.

Fig. 15a shows a large variability in fatigue properties. However, when comparing to the respective YTS Fig. 15b, most of the results show fatigue strength between 10^6 and 10^7 cycles to be close to 100% of the YTS, except this study's as-built LPBF and LPBF samples from Koutiri et al. [48]. Indeed, those are the only as-built near-net-shape samples (not machined and just polished). It therefore appears that a polishing step alone is not sufficient to remove the defect-dense area near the surface of the sample, which is detrimental to fatigue life. However, heat treatment improves the defects tolerance of the LPBF microstructure and raises his fatigue strength to 100% of the YTS.

The impact of defects on the self-heating response of metallic materials is subject to discussions in the literature, but no firm conclusion has been reached. Defects are often considered as preferential sites for microplasticity in the models used to explore self-heating experimental results and predict fatigue life [35], but their impact on the self-heating curve shape were not discussed. Bercelli et al. [52] showed that the rare defects detected in a WAAM bronze-Al alloy had no impact on the experimental self-heating curves. Balit et al. [18] showed different self-heating curves for vertical and horizontal 316L steel DED samples and

attributed the difference to the interlayer defects. In this study, the self-heating fatigue limit and the fatigue strength, expressed in terms of maximum stress at $2.2 \cdot 10^6$ cycles for as-built and heat-treated DED and hybrid samples are comparable, and close to the respective yield tensile stress of the material (Table 4). All those samples were machined and polished. In the case of as-built LPBF samples, this fatigue strength is below 250 MPa, while the self-heating tests identified a theoretical fa-tigue limit around 600 MPa, close to 100% YTS. After the heat treat-ment, the gap is reduced but remains. All LPBF samples were tested as polished near-net shape samples. In addition, the self-heating results from this study's LPBF samples show a different trend compared to DED samples (Fig. 12). The increases of the sample's temperature are significantly higher than the asymptotes in the transition between the first and second regime. These premature temperature raises can be attributed to the localization of plasticity at the tip of the defects, causing heat dissipation prone to increase the global temperature of the sample before the generalization of microplasticity. The presence of harmful defects is hence detectable by the self-heating method.

Yet, the theoretical analysis of the two regimes to determine the fatigue limit is not suitable to the LPBF Inconel 625 microstructure with defects. Using the first temperature increase, asymptote of the transition, or monitoring local temperature fields would be interesting per-spectives to capture the impact of defects by self-heating. Furthermore, the transition between the two regimes could be representative of the defects and their impact on the fatigue strength of metallic materials.

4.2. Initiation and propagation mechanisms in hybrid specimen

The crack leading to the fatigue failure of the hybrid specimen always initiated on a defect. When the failure happened at the LPBF-DED interface, a circular lack of fusion was observed. When the initiation took place in the DED section, Marangoni defects [42] were observed (Fig. 10). On the S-N plot Fig. 9, the samples that failed at the interface or in the DED section present similar fatigue lives and similar dispersion. The type of initiation and its localization does not affect the fatigue life of the samples. Only the as-built samples that were solicited at high load levels (greater than 450 MPa) display a shorter fatigue life than the mono-process samples.

For higher load levels, the contribution to fatigue life is mainly coming from the crack propagation compared to the crack initiation [43,44]. The samples that had a shorter fatigue life at high load levels both failed at the LPBF-DED interface, and both displayed a large circular lack-of-fusion mentioned above (Fig. 10). The shape and size of this defect induced stress concentration throughout the crack propagation and caused the fatigue life to drop. The propagation mechanisms observed in the hybrid samples Fig. 11 were identical to that observed in mono-process samples [30].

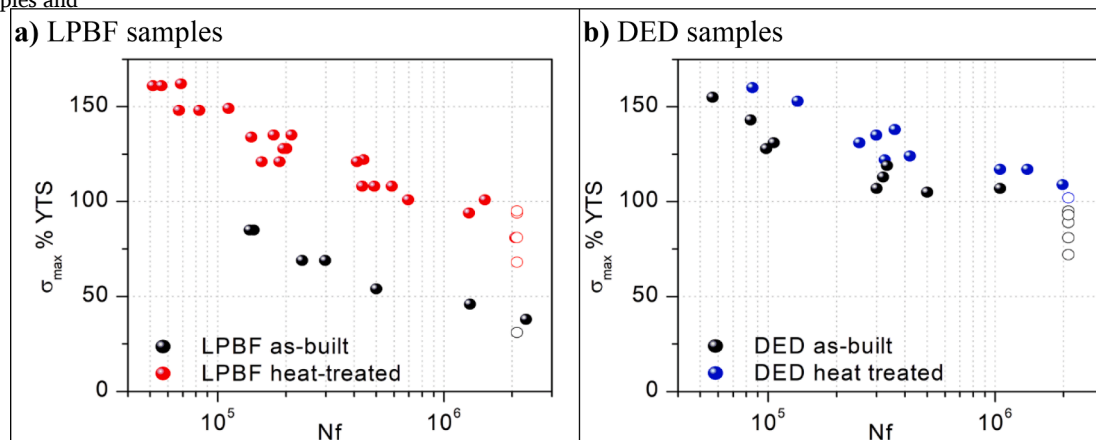


Fig. 14. S-N plots of a) LPBF b) DED as-built and heat-treated samples: the maximum stresses were standardized by their respective yield tensile stresses.

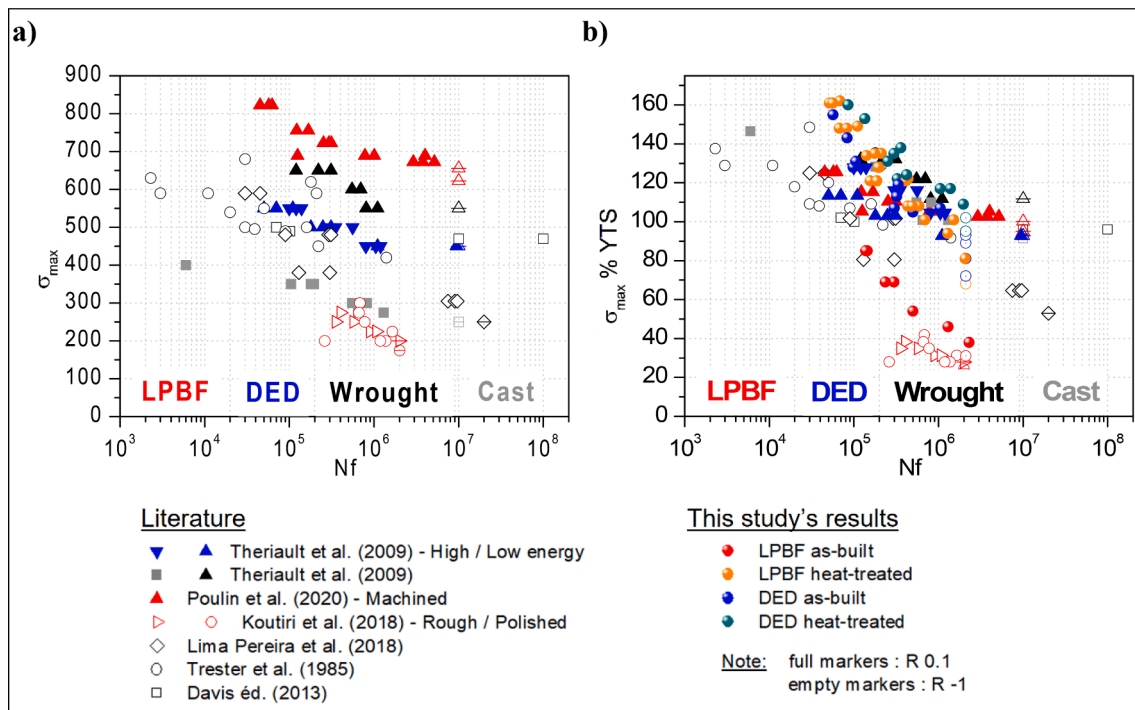


Fig. 15. Comparative S-N plots of fatigue properties of Inconel 625 made by various process: Results from this study and literature represented by a) maximal stress, b) maximal stress standardized by the respective YTS [46–51].

For lower solicitation levels, the initiation step is preponderant, and no clear difference between mono-process and hybrid sample fatigue resistance were observed. Further tests of crack propagation monitoring could confirm this impact of the large defects in the samples section on the fatigue life. In addition, the fatigue resistance of metallic alloys has been mostly studied on samples with homogeneous characteristics. The hybrid samples studied here have two sections with a significant gap in properties and behavior, for example strain–stress relations. The description of initiation, propagation and final failure might not be adequate to describe fully the fatigue resistance of hybrid samples.

4.3. Impact of heterogeneous mechanical properties on fatigue strength

The self-heating tests suggest that the Inconel 625 microstructure induced by LPBF, as-built or heat-treated, should have significantly higher fatigue resistance than the DED microstructure. Yet, the fatigue properties of as-built, near-net-shape LPBF samples are significantly limited by the presence of lacks of fusions around the surface of samples, and their fatigue strength are lower than that of the DED's. The heat-treated microstructure exhibits a better accommodation capacity, but the fatigue strength, expressed in terms of maximum stress at $2.2 \cdot 10^6$ cycles, remains slightly lower than that of DED's (Fig. 9b). Despite this superiority of the DED microstructure compared to the LPBF micro-structure when measured on mono-process samples, the failure of hybrid samples systematically occurs in the DED section, or at the interface. In both cases, defects were observed to cause the crack initiation: lacks of fusion at the interface or Marangoni pores in the DED section. Both are related to the process control of DED deposition.

But the difference of microstructure between LPBF and DED is also responsible. The cyclic stress-controlled tests of hybrid samples monitored with strain gauges illustrated in Fig. 8 show immediate strain localization in the DED section, which concentrates most of the accumulated plastic strain. This is due to the lower yield tensile stress of the DED. In addition, the DED section is subject to higher hardening and dissipates more energy than the LPBF section. This is consistent with the self-heating results, where the increases in temperature are higher for

the DED section despite the heat transfers between the two sections. In the ideal case of defect-free hybrid samples, it is assumed that the failure would still occur systematically in the DED section due to the strain localization and unbalanced energy dissipation.

In addition, the gauges measured only the axial normal strain. Shear strains could be induced by the gradient of properties between the LPBF substrate and DED deposition and could also explain the preferential failure of hybrid samples at the interface. Further investigations on thinner and flat test samples monitored with strain fields and temperature field measurement could be of great interest to better understand the challenge of samples with heterogeneous properties.

The heat treatment was shown to increase the ductility of the samples, especially for the LPBF Inconel 625 microstructure [30]. It also reduces the gap between the static tensile properties of LPBF and DED, which increases the mechanical resistance of hybrid samples. For cyclic loading, the heat treatment reduced the difference in plastic strain accumulation between the LPBF and the DED sections. However, a significant difference remains and the DED dissipated more energy thus displaying the lowest fatigue strength. As for the static tensile properties, the hybrid samples' fatigue resistance was limited by the DED section but benefited from similar properties. The fatigue strength of hybrid samples is equivalent to that of the DED mono-process parts.

5. Conclusion

The simultaneous investigation of the fatigue behavior of mono-process LPBF or DED Inconel 625 with samples produced by LPBF-DED hybridization allowed to identify the impact of each process on fatigue strength of hybrid samples. The effects of the specific LPBF and DED microstructures were explained through the investigation of as-built and heat-treated states. In addition, the study involved near-net-shaped and machined samples, which permitted to analyze the impact of near-surface defects on LPBF fatigue behavior. Addressing these multiple effects allowed to draw three main conclusions on fatigue behavior of LPBF and DED Inconel 625, as well as a benchmark for hybrid LPBF-DED process:

- The fatigue strength of hybrid LPBF-DED parts was identical to that of the weakest section, which in the particular case of machined samples is the DED section. The transition between LPBF and DED microstructures was not the limiting factor and did not weaken the properties of as-built, nor of heat treated samples.
- The near-surface defects are the main limiting factors in the fatigue life of LPBF or DED samples, mono-process or hybrid. The near-net-shape LPBF samples showed systematic initiation on defects and machined hybrid samples tested showed initiation on near-surface lacks of fusion or Marangoni defects.
- The recrystallization provided by heat treatment successfully increased the defects tolerance of the LPBF and DED microstructures. The fatigue strength, expressed in terms of maximum stress at $2.2 \cdot 10^6$ cycles, was close to 100 % of the YTS for heat treated LPBF, DED and hybrid samples, which was consistent with results reported in the literature [46–51]. In addition, the heat treatment reduced drastically the gap between LPBF and DED microstructures. In addition to this investigation of the fatigue behavior of hybrid

LPBF-DED Inconel 625, this paper points out the following perspectives:

- Combining the self-heating techniques with a local strain field measurement could provide additional information on the fatigue resistance and weaknesses of the samples. The proposed link between the self-heating regimes' transition and the presence of large defects must be validated and numerical modelling should be proposed to analyse fatigue self-heating curves.
- The surface of the LPBF samples were polished, while the hybrid specimens were machined. A comparison of LPBF mono-process machined samples could help in determining the exact impact of the surface defects and roughness.
- The LPBF-DED interface and local complex strains generated (in particular shear strain) could be quantified.
- The DED process could be optimized to limit the difference in microstructures between the LPBF and DED sections of hybrid samples and homogenize even further the mechanical and fatigue properties.

Declaration of Competing Interest

The authors declare that they have no known competing financial interests or personal relationships that could have appeared to influence the work reported in this paper.

Data availability

Data will be made available on request.

Acknowledgements

This work was financed and supported by Segula Technologies.

References

- [1] Leino M, Pekkarinen J, Soukka R. The role of laser additive manufacturing methods of metals in repair, refurbishment and remanufacturing - Enabling circular economy. *Phys Procedia* 2016;83:752–60. <https://doi.org/10.1016/j.phpro.2016.08.077>.
- [2] Wilson JM, Piya C, Shin YC, Zhao F, Ramani K. Remanufacturing of turbine blades by laser direct deposition with its energy and environmental impact analysis. *J Clean Prod* 2014;80:170–8. <https://doi.org/10.1016/j.jclepro.2014.05.084>.
- [3] Jones J, McNutt P, Tosi R, Perry C, Wimpenny D. Remanufacture of turbine blades by laser cladding, machining and in-process scanning in a single machine. 23rd International Solid Freeform Fabrication Symposium, vol. 39, 2012.
- [4] Zhang X, Cui W, Li W, Liou F. Metallic components repair strategies using the hybrid manufacturing process. In: 28th International Solid Freeform Fabrication Symposium; 2017. p. 1862–76.
- [5] Wohlers T, Caffrey T. Wohlers Report 2018. 2018.
- [6] Leandro P, Leandro S. Sculpteo dévoile son étude annuelle sur les tendances du marché de l'impression 3D 2017. <https://www.sculpteo.com/media/press/2017/09/04/CP%20Sculpteo%20State%20of%203Dprinting%20FR%202018%20.pdf> (accessed December 21, 2022).

- [7] Buchanan C, Gardner L. Metal 3D printing in construction: a review of methods, research, applications, opportunities and challenges. *Eng Struct* 2019;180:332–48. <https://doi.org/10.1016/j.engstruct.2018.11.045>.
- [8] Graf B, Schuch M, Kersting R, Gumenyuk A, Rethmeier M. Additive process chain using selective laser melting and laser metal deposition. *Lasers in Manufacturing* 2015;2015:59.
- [9] Gao W, Zhang Y, Ramanujan D, Ramani K, Chen Y, Williams CB, et al. The status, challenges, and future of additive manufacturing in engineering. *CAD Computer Aided Design* 2015;69:65–89. <https://doi.org/10.1016/j.cad.2015.04.001>.
- [10] Zhang L, Zhang S, Zhu H, Hu Z, Wang G, Zeng X. Horizontal dimensional accuracy prediction of selective laser melting. *Mater Des* 2018;160:9–20. <https://doi.org/10.1016/j.matdes.2018.08.059>.
- [11] Gibson I, Rosen D, Stucker B. *Additive Manufacturing Technologies*. Springer, US 2015. https://doi.org/10.1007/978-3-642-35950-7_16866-1.
- [12] Godec M, Malej S, Feizpour D, Donik, Balažić M, Klobčar D, et al. Hybrid additive manufacturing of Inconel 718 for future space applications. *Mater Charact* 2021; 172. <https://doi.org/10.1016/j.matchar.2020.110842>.
- [13] BeAM. Case Study: Hybrid Piston - BeAM Machines - Directed Energy Deposition 2019. <https://www.beam-machines.com/internal/case-study-hybrid-piston> (accessed July 4, 2019).
- [14] Qin LY, Men JH, Zhang LS, Zhao S, Li CF, Yang G, et al. Microstructure homogenizations of Ti-6Al-4V alloy manufactured by hybrid selective laser melting and laser deposition manufacturing. *Mater Sci Eng A* 2019;759:404–14. <https://doi.org/10.1016/j.msea.2019.05.049>.
- [15] Oh WJ, Lee WJ, Kim MS, Jeon JB, Shim DS. Repairing additive-manufactured 316L stainless steel using direct energy deposition. *Opt Laser Technol* 2019;117:6–17. <https://doi.org/10.1016/j.optlastec.2019.04.012>.
- [16] Pinkerton AJ, Wang W, Li L. Component repair using laser direct metal deposition. *J Eng Manuf* 2008;222:827–36. <https://doi.org/10.1243/09544054JEM1008>.
- [17] Liu Q, Wang Y, Zheng H, Tang K, Ding L, Li H, et al. Microstructure and mechanical properties of LMD-SLM hybrid forming Ti6Al4V alloy. *Mater Sci Eng A* 2016;660: 24–33. <https://doi.org/10.1016/j.msea.2016.02.069>.
- [18] Balit Y, Joly LR, Szymtka F, Durbecq S, Charkaluk E, Constantinescu A. Self-heating behavior during cyclic loadings of 316L stainless steel specimens manufactured or repaired by Directed Energy Deposition. *Mater Sci Eng A* 2020;786:139476. <https://doi.org/10.1016/j.msea.2020.139476>.
- [19] Soffel F, Eisenbarth D, Hosseini E, Wegener K. Interface strength and mechanical properties of Inconel 718 processed sequentially by casting, milling, and direct metal deposition. *J Mater Process Technol* 2021;291:117021. <https://doi.org/10.1016/j.jmatprotec.2020.117021>.
- [20] Marchese G, Garmendia Colera X, Calignano F, Lorusso M, Biamino S, Minetola P, et al. Characterization and Comparison of Inconel 625 Processed by Selective Laser Melting and Laser Metal Deposition. *Adv Eng Mater* 2017;19:1–9. <https://doi.org/10.1002/adem.201600635>.
- [21] Nguejio J, Szymtka F, Hallais S, Tanguy A, Nardone S, Godino MM. Comparison of microstructure features and mechanical properties for additive manufactured and wrought nickel alloys 625. *Mater Sci Eng A* 2019;764:138214. <https://doi.org/10.1016/j.msea.2019.138214>.
- [22] Dinda GP, Dasgupta AK, Mazumder J. Laser aided direct metal deposition of Inconel 625 superalloy: Microstructural evolution and thermal stability. *Mater Sci Eng A* 2009;509:98–104. <https://doi.org/10.1016/j.msea.2009.01.009>.
- [23] Gong J, Wei K, Liu M, Song W, Li X, Zeng X. Microstructure and mechanical properties of AlSi10Mg alloy built by laser powder bed fusion/direct energy deposition hybrid laser additive manufacturing. *Addit Manuf* 2022;59 doi: 10.1016/j.addma.2022.103160.
- [24] Uhlmann E, Dürchtig J, Petrat T, Krohmer E, Graf B, Rethmeier M. Effects on the distortion of Inconel 718 components along a hybrid laser-based additive manufacturing process chain using laser powder bed fusion and laser metal deposition. *Progress in Additive Manufacturing* 2021;6:385–94. <https://doi.org/10.1007/s40964-021-00171-9>.
- [25] Li KK, Chen MS, Lin YC, Yuan WQ. Microstructural evolution of an aged Ni-based superalloy under two-stage hot compression with different strain rates. *Mater Des* 2016;111:344–52. <https://doi.org/10.1016/j.matdes.2016.09.007>.
- [26] Guévenoux C, Hallais S, Balit Y, Charles A, Charkaluk E, Constantinescu A. Plastic strain localization induced by microstructural gradient in laser cladding repaired structures. *Theoretical and Applied Fracture Mechanics* 2020;107 doi: 10.1016/j.tafmec.2020.102520.
- [27] Martin N, Hor A, Copin E, Lours P, Ratsifandrihana L. Correlation between microstructure heterogeneity and multi-scale mechanical behavior of hybrid LPBF-DED Inconel 625. *J Mater Process Technol* 2022;303 doi: 10.1016/j.jmatprotec.2022.117542.
- [28] Malej S, Medved J, Batič BŠ, Tehovnik F, Vode F, Burja J, et al. The influence of segregation bands and hot rolling on the precipitation of secondary phases during aging at 750 °C for nickel alloy 625. *Metals (Basel)* 2019;9 doi: 10.3390/met9030314.
- [29] Gao Y, Ding Y, Li H, Dong H, Zhang R, Li J, et al. Grain-size dependent elastic-plastic deformation behaviour of inconel 625 alloy studied by in-situ neutron diffraction. *Intermetallics (Barking)* 2021;138:107340. <https://doi.org/10.1016/j.intermet.2021.107340>.
- [30] Martin N, Hor A, Copin E, Lours P, Ratsifandrihana L. Impact of annealing treatment on the fatigue behavior of Inconel 625 produced by laser-based powder bed fusion. *Fatigue Fract Eng Mater Struct* 2022;1–18. <https://doi.org/10.1111/ffe.13648>.

- [31] Stinville JC, Charpagne MA, Cervellon A, Hemery S, Wang F, Callahan PG, et al. On the origins of fatigue strength in crystalline metallic materials. *Science* 1979;2022 (377):1065–71. <https://doi.org/10.1126/science.abn0392>.
- [32] Florin P, Facchinetti M, Doudard C, Calloch S. Fast Fatigue Properties Identification by “Self-heating” Method: Application to Automotive Welded Joints. *Procedia Eng* 2013;66:676–83. <https://doi.org/10.1016/j.proeng.2013.12.120>.
- [33] Ezanno A, Doudard C, Calloch S, Heuzé JL. A new approach to characterizing and modeling the high cycle fatigue properties of cast materials based on self-heating measurements under cyclic loadings. *Int J Fatigue* 2013;47:232–43. <https://doi.org/10.1016/j.ijfatigue.2012.09.005>.
- [34] Doudard C, Calloch S, Cugy P, Galtier A, Hild F. A probabilistic two-scale model for high-cycle fatigue life predictions. *Fatigue Fract Eng Mater Struct* 2005;28:279–88. <https://doi.org/10.1111/j.1460-2695.2005.00854.x>.
- [35] Ezanno A, Doudard C, Calloch S, Millot T, Heuzé JL. Fast characterization of high-cycle fatigue properties of a cast copperaluminum alloy by self-heating measurements under cyclic loadings. *Procedia Eng* 2010;2:967–76. <https://doi.org/10.1016/j.proeng.2010.03.105>.
- [36] Amini B, Demmouche Y, Barati M, Helbert G, Chirani SA, Calloch S. Self-heating of metastable 304L austenitic stainless steel under cyclic loading: Influence of initial martensite volume fraction, testing temperature and pre-strain. *Mech Mater* 2020; 151. <https://doi.org/10.1016/j.mechmat.2020.103596>.
- [37] Peyrac C, Jollivet T, Leray N, Lefebvre F, Westphal O, Gornet L. Self-heating Method for Fatigue Limit Determination on Thermoplastic Composites. *Procedia Eng*, vol. 133, Elsevier Ltd; 2015, p. 129–35 doi: 10.1016/j.proeng.2015.12.639.
- [38] Doudard C, Poncelet M, Calloch S, Boue C, Hild F, Galtier A. Determination of an HCF criterion by thermal measurements under biaxial cyclic loading. *Int J Fatigue* 2007;29:748–57. <https://doi.org/10.1016/j.ijfatigue.2006.06.009>.
- [39] Gornet L, Sudevan D, Rozycki P. A study of various indicators to determine the fatigue limit for woven carbon/epoxy composites under self heating methodology. *Procedia Eng* 2018;213:161–72. <https://doi.org/10.1016/j.proeng.2018.02.018>.
- [40] Roué V, Doudard C, Calloch S, Montel F, Pujol D'Andrebo Q, Corpace F. Rapid determination of the high cycle fatigue properties of high temperature aeronautical alloys by self-heating measurements. *MATEC Web of Conferences* 2018;165:1–9. <https://doi.org/10.1051/mateconf/201816522022>.
- [41] Liang X, Hor A, Robert C, Salem M, Morel F. Correlation between microstructure and cyclic behavior of 316L stainless steel obtained by Laser Powder Bed Fusion. *Fatigue Fract Eng Mater Struct* 2022;45:1505–20. <https://doi.org/10.1111/ffe.13684>.
- [42] Gao Y, Zhao J, Zhao Y, Wang Z, Song H, Gao M. Effect of processing parameters on solidification defects behavior of laser deposited AlSi10Mg alloy. *Vacuum* 2019; 167:471–8. <https://doi.org/10.1016/j.vacuum.2019.06.042>.
- [43] Rackwitz J, Yu Q, Yang Y, Laplanche G, George EP, Minor AM, et al. Effects of cryogenic temperature and grain size on fatigue-crack propagation in the medium-entropy CrCoNi alloy. *Acta Mater* 2020;200:351–65. <https://doi.org/10.1016/j.actamat.2020.09.021>.
- [44] Zhu X, Gong C, Jia YF, Wang R, Zhang C, Fu Y, et al. Influence of grain size on the small fatigue crack initiation and propagation behaviors of a nickel-based superalloy at 650 °C. *J Mater Sci Technol* 2019;35:1607–17. <https://doi.org/10.1016/j.jmst.2019.03.023>.
- [45] Yadollahi A, Shamsaei N. Additive manufacturing of fatigue resistant materials: Challenges and opportunities. *Int J Fatigue* 2017;98:14–31. <https://doi.org/10.1016/j.ijfatigue.2017.01.001>.
- [46] Theriault A, Xue L, Dryden J. Fatigue behavior of laser consolidated IN-625 at room and elevated temperatures. *Mater Sci Eng A* 2009;516:217–25. <https://doi.org/10.1016/j.msea.2009.03.056>.
- [47] Poulin JR, Kreitzberg A, Terriault P, Brailovski V. Fatigue strength prediction of laser powder bed fusion processed Inconel 625 specimens with intentionally-seeded porosity: Feasibility study. *Int J Fatigue* 2020;132:105394. <https://doi.org/10.1016/j.ijfatigue.2019.105394>.
- [48] Koutiri I, Pessard E, Peyre P, Amlou O, de Terris T. Influence of SLM process parameters on the surface finish, porosity rate and fatigue behavior of as-built Inconel 625 parts. *Journal of Materials Processing Tech* 2018;255:536–46. <https://doi.org/10.1016/j.jmatprotec.2017.12.043>.
- [49] Lima Pereira FG, Lourenço JM, do Nascimento RM, Castro NA. Fracture behavior and fatigue performance of inconel 625. *Mater Res* 2018;21. <https://doi.org/10.1590/1980-5373-MR-2017-1089>.
- [50] Trester P, Kaae J, Gallix R. Fatigue Strength of Inconel 625 plate and weldments used in the DIII-D configuration vacuum vessel. *J Nucl Mater* 1985;134:347–50.
- [51] ASM Specialty Handbook: Nickel, Cobalt, and Their Alloys 2013;vol. 38. <https://doi.org/10.1361/ncta2000p003>.
- [52] Bercelli L, Moyné S, Dhondt M, Doudard C, Calloch S, Beaudet J. A probabilistic approach for high cycle fatigue of Wire and Arc Additive Manufactured parts taking into account process-induced pores. *Addit Manuf* 2021;42. <https://doi.org/10.1016/j.addma.2021.101989>.